Submitted to *Journal of the European Ceramic Society*, December 2019. Revised February 2020.

Processing of orthotropic and isotropic superhard B_4C composites reinforced with reduced graphene oxide

Cristina Ojalvo [a], Rodrigo Moreno [b], Fernando Guiberteau [a], Angel L. Ortiz [a,*]

[a] Departamento de Ingeniería Mecánica, Energética y de los Materiales, Universidad de Extremadura, 06006 Badajoz, Spain.

[b] Instituto de Cerámica y Vidrio, Consejo Superior de Investigaciones Científicas, Madrid 28049, Spain.

Abstract

A fabrication route based on aqueous colloidal processing plus transient liquid-phase assisted spark-plasma-sintering (SPS) with Ti-Al additives is described for the environmentally friendly obtention of superhard B_4C composites reinforced with reduced graphene oxide (rGO) having orthotropic and isotropic microstructures. It is shown that the former, which have coarse rGO platelets preferentially aligned perpendicular to the SPS pressing direction, can be prepared from mixtures of B_4C and Ti-Al particles with a source of thick, large rGO nanoplatelets by imposing smooth co-dispersion conditions to avoid platelet re-exfoliation and fragmentation. The latter, which have fine rGO platelets randomly oriented, can be fabricated from mixtures of B_4C and Ti-Al particles with a source of thin, small rGO nanoplatelets by applying intensive sonication to promote platelet re-exfoliation and fragmentation during co-dispersion. Finally, it is shown that these orthotropic and isotropic B_4C/rGO composites are equally superhard, and that, as expected, their microstructures interact differently with the cracks. Finally, this processing route is simple, and easily adaptable/extensible to make other ceramic/rGO composites with orthotropic and isotropic microstructures.

Keywords: B_4C; aqueous colloidal processing; spark-plasma sintering; microstructural design; mechanical properties.

* Corresponding author:

Angel L. Ortiz
Phone: +34 924289600 Ext: 86726
Fax: +34 924289601
E-mail: alortiz@unex.es

1. Introduction

B_4C-based ceramics are receiving growing attention lately as one of the most promising types of structural material for use in contact-mechanical and tribological applications [1-10]. What makes B_4C particularly appealing over other advanced structural ceramics is its super-hardness and ultra-lightweight, which are very important attributes in many structural applications (essential for example in the field of personnel and vehicle armour). Despite their great promise as advanced structural ceramics, widespread implementation of B_4C-based ceramics is still very limited because they are hard to sinter [4,11] and brittle [1,12]. The former is mitigated using sintering aids [4,13,14] and/or non-conventional sintering (in particular, spark-plasma sintering (SPS)) [15-20]. The latter is palliated by forcing cracks to in some way interact intensely with the microstructure (microstructural toughening) [21,22].

Following the classical approach of toughening brittle ceramics with fibres, whiskers, and platelets [21,22], it is today more popular to use carbon nanostructures as reinforcements. These include zero-dimensional (0-D) carbon nanoparticles (CNPs), one-dimensional (1-D) carbon nanotubes (CNTs), and two-dimensional (2-D) graphene nanoplatelets or their 2-D derivatives (i.e., nanoplatelets of graphene oxide (GO), partially-reduced graphene oxide (prGO), or reduced graphene oxide (rGO)). CNPs have little toughening effect, but act efficiently as internal solid lubricants in wear applications [23]. CNTs, however, have been widely used as toughening reinforcements [24,25], and it has been revealed that they exhibit a unique crack-bridging toughening mechanism [26]. Reinforcement with 2-D carbon nanoplatelets has been far less studied despite their being in principle potentially more effective in bridging cracks [27] and more easily dispersible in ceramic matrices [24]. Very recently, novel *in situ* observations of crack propagation in Al_2O_3 ceramics reinforced with rGO nanoplatelets have identified why

these composites are tougher, and have shown the marked importance of the size and orientation of those nanoplatelets [28]. The ceramic/rGO composites are sometimes unintentionally "orthotropic" because the uniaxial pressure applied during SPS results naturally in microstructures with rGO nanoplatelets aligned perpendicularly to the compaction direction. Others, however, are fortuitously isotropic. Importantly, it has been shown that the orthotropic ceramic composites reinforced with coarse rGO nanoplatelets are markedly tough for cracks propagating with their front normal to the rGO nanoplatelets [28], while the isotropic ceramic composites reinforced with randomly-oriented fine rGO nanoplatelets are moderately tough in all directions [28].

B_4C is no exception, and, although few, there have already been studies on B_4C/rGO composites reporting both orthotropic and isotropic microstructures. They have, however, been fabricated somewhat uncontrollably by very varied processing routes (heterogeneous co-precipitation plus ex-situ reduction and SPS [29], self-assembly polymerization plus SPS [30], high-energy rotary-vibratory milling plus hot-pressing [31-34], ultrasonic dispersion plus hot-pressing [35], attrition milling plus hot-pressing [36], diluted wet-dispersion plus SPS [37], etc.), some of which are certainly complex. It thus appeared especially timely to explore how to turn the orthotropic and isotropic microstructural designs into reality for B_4C/rGO by one given simple processing route, in a controlled manner. This was indeed the objective of the present study, which is specifically aimed at developing an environmentally friendly fabrication route combining aqueous colloidal processing with transient liquid-phase assisted SPS of B_4C with Ti-Al additives that enables the controlled obtention of one or the other microstructure depending on the source of rGO nanoplatelets and on the conditions of colloidal co-dispersion used. The motivation for processing controllably these types of B_4C/rGO composites is because toughened,

superhard materials based on B_4C have great potential for myriad of engineering applications, and the ceramics industry demands fabrication processes for the mass production of parts that are well established.

2. Experimental procedure

2.1. Aqueous colloidal processing of the powder mixtures

The starting materials were commercially available powders of B_4C (Grade HD 20, H.C. Starck, Germany), Ti-Al (22895, Alfa Aesar, Germany), GO (1.8, Abalonyx AS, Norway), and prGO (2.1, Abalonyx AS, Norway) with the features indicated in Table 1, as well as a commercially available cationic polyelectrolyte (polyethylenimine (PEI); MW ~25,000; Sigma-Aldrich, USA). Note that (*i*) Ti-Al is the transient liquid-phase sintering additive for B_4C [38,39], and that (*ii*) GO and prGO are the source of rGO for the orthotropic and isotropic B_4C/rGO composites, respectively. From these four powders, mixtures of B_4C+Ti-Al+GO and B_4C+Ti-Al+prGO, designed to yield B_4C composites with 4.9 vol.% Ti-Al and 2 vol.% rGO, were prepared by aqueous colloidal processing, as described below. These concentrations of Ti-Al and rGO were chosen because earlier studies have shown that they optimize the SPS densification [38] and mechanical properties [29], respectively, of the B_4C composites.

Firstly, the appropriate proportion (wt.%) of PEI deflocculant for dispersing the GO/prGO powder in water at neutral pH was identified by studies of colloidal stability through zeta potential measurements (Zetasizer Nano-ZS, Malvern, UK). These measurements were done on dilute aqueous suspensions (0.1 g/l; KCl 10^{-2} M as inert electrolyte) of the GO/prGO powders without and with different PEI additions, after their sonication for 1 min and equilibration for

<10 min. The colloidal stability in water of the B_4C and Ti-Al powders is already known [40], and therefore the study was not repeated.

Secondly, the appropriate homogenization conditions for preparing at neutral pH aqueous suspensions of both B_4C+Ti-Al+GO and B_4C+Ti-Al+prGO as concentrated as possible were identified by rheological studies (MARS, Haake, Thermo, Germany). These studies were performed on suspensions with different total solids loadings, prepared under continuous mechanical agitation (at 310 rpm) according to the following sequence: (1) addition to the de-ionized water of the PEI content required to disperse the GO/prGO powder, and agitation for 1 min; (2) gradual incorporation of the GO/prGO powder, and agitation for 5 min; (3) addition of the PEI content required to disperse the Ti-Al and B_4C powders, and agitation for 1 min; (4) introduction of the Ti-Al powder, and agitation for 15 min; and (4) gradual addition of the B_4C powder, adjustment of the pH to neutral pH, agitation for 30 min, and pulsed sonication (UP-400S, Hielscher Ultrasonics GmbH, Germany) at 240 W for the desired time. The flow curves were measured operating the rheometer, configured in the double cone-plate geometry, in controlled shear rate mode (from 0 to 1000 s^{-1} in 300 s, then a plateau at 1000 s^{-1} for 60 s, and lastly from 1000 to 0 s^{-1} also in 300 s).

Lastly, the optimal concentrated suspensions of B_4C+Ti-Al+GO and B_4C+Ti-Al+prGO were frozen using a rotary evaporator (RV10 basic, IKA, Germany) immersed in a liquid-N_2 bath, and then were freeze-dried (Cryodos-50, Telstar, Spain) at -50 °C and 0.3 mPa for 24 h. The resulting powder mixtures were characterized by Raman spectroscopy (Nicolet Almega XR, Thermo Scientific, UK).

2.2. Spark-plasma sintering of the B_4C/rGO composites

The powder mixtures of B_4C+Ti-Al+GO and B_4C+Ti-Al+prGO were loaded individually into graphite dies (2-cm diameter) lined with graphite foils and covered by graphite blankets, and were SPS-ed in dynamic vacuum. The SPS conditions were those already used successfully in B_4C ceramics with Ti-Al [40]: target temperature of 1900 °C (as measured using an axial optical pyrometer), heating ramp of 100 °C/min, soaking time of 30 min, and pressure of 75 MPa (applied at 300 °C). The resulting B_4C composites were characterized microstructurally by scanning electron microscopy (SEM; Quanta 3D, FEI, The Netherlands) at the fracture surfaces, and Raman spectroscopy at polished, top surfaces. They were also characterized mechanically by Vickers indentation (MV-1, Matsuzawa, Japan) at 9.8 N load. Two types of tests were done, ones on the polished, top surface to evaluate the hardness (10 indents per sample) [21] and others on the gold-coated, polished cross-section surface to elucidate how the Vickers cracks interacted with the microstructures. The observations of the residual Vickers indents were performed in all cases by optical microscopy (OM; Epiphot 300, Nikon, Japan). The Vickers indents were also selectively observed by SEM (S-3600N, Hitachi, Japan).

3. Results and discussion

The environmentally friendly fabrication of the orthotropic and isotropic superhard B_4C/rGO composites developed here comprises the steps of aqueous colloidal processing and SPS described next.

3.1. Aqueous colloidal processing of B_4C+Ti-Al+GO/prGO powder mixtures

Fig. 1 shows the dependence of the zeta potential on pH for the individual dilute aqueous suspension of GO without and with different PEI additions. It is clear that GO is negatively

charged over the entire range of pHs investigated, either with no isoelectric point or with one at a very acidic pH (pH<2). It is also seen that the zeta potential increases relatively little in magnitude with pH, and is (in absolute value) always greater than 30 mV. In principle, GO would then be colloidally stable in water at practically any pH. This is because this GO is inherently functionalized with hydroxyl, carbonyl, epoxy, and alcoxy surface groups with a C:O ratio of 2.4-2.6, and so is hydrophilic and easily dispersible in water. Nonetheless, unfortunately it is not possible to prepare well-dispersed aqueous suspensions of B_4C+Ti-Al+GO at neutral pH because B_4C and Ti-Al are not colloidally stable (due to their low zeta potentials) [40]. Indeed, it has recently been demonstrated that the aqueous concentrated suspensions of B_4C+Ti-Al are well dispersed at neutral pH if deflocculated with a cationic polyelectrolyte [40], conditions at which the B_4C and Ti-Al particles are charged positively with zeta potentials of ~50 mV (see Fig. 1). Introducing GO into these suspensions would then result in the undesirable hetero-aggregation, not in the sought-for co-dispersion, of the negatively-charged GO nanoplatelets with the positively-charged B_4C and Ti-Al particles.

Logically, it is possible to change the charge of GO from negative to positive by cationic polyelectrolytes, and in particular by PEI which would thus simplify the route of colloidal processing (because PEI is the deflocculant used for B_4C and Ti-Al [40]). Accordingly, Fig. 1 also shows the evolution of the zeta potential as a function of pH for the individual dilute suspension of GO with different PEI additions. Clearly, only 1 wt.% PEI already induces the appearance of an isoelectric point for GO at pH~4.2, but it is insufficient for preparing well-dispersed suspensions of B_4C+Ti-Al+GO at neutral pH because at this pH GO still has a negative zeta potential (-45 mV), not positive as do B_4C and Ti-Al [40]. With increasing PEI content, the isoelectric point of GO gradually shifts to greater pH (pH~6.5, 7.0, 7.2, 8.0, 9.3, and 9.7 for PEI

contents of 2, 3, 4, 6, 8, and 10 wt.%, respectively) while the zeta potential below the isoelectric point increases markedly, which is clear evidence for electrosteric stabilization. More importantly, it is seen that ~8 wt.% PEI already provides GO with the required (positive) zeta potential of ~50 mV exhibited by B_4C [40] and Ti-Al [40] with 1 wt.% PEI at neutral pH.

Fig. 2 shows the dependence of the zeta potential on pH for the individual dilute aqueous suspension of prGO without and with different PEI additions. It is seen that, unlike GO, prGO exhibits an isoelectric point at pH~2.6. This is because this prGO was prepared by the thermal reduction of GO at 400 °C, which resulted in the partial removal of oxygen-containing functional groups (prGO thus has less hydroxyl, carbonyl, and epoxy groups than GO, as well as a much higher C:O ratio of 7-8). Nonetheless, neither can prGO be used directly for preparing well-dispersed suspensions of B_4C+Ti-Al+prGO at neutral pH because, like GO, at this pH its zeta potential is still negative (-40 mV) [40]. Consequently, adding PEI is also necessary in this case. This is especially the case given the very hydrophobic nature of prGO, and its consequent low dispersibility in water. As expected, PEI addition gradually shifts the isoelectric point of prGO to greater pH (pH~4.6, 6.0, 9.3, and 10.0 for PEI contents of 1, 2, 4, and 6 wt.%, respectively). Indeed, prGO and GO have similar isoelectric points for low PEI contents (i.e., 1 and 2 wt.%), above which prGO has much higher isoelectric points. Interestingly, ~6 wt.% PEI already provides prGO with the required (positive) zeta potential of ~50 at neutral pH, which is ~2 wt.% PEI less than for GO.

Well-dispersed concentrated suspensions of B_4C+Ti-Al+GO and B_4C+Ti-Al+prGO will then be prepared at neutral pH (pH~6.9-7.0) by adding 8 wt.% PEI for GO, 6 wt.% PEI for prGO, and 2 wt.% PEI for both B_4C and Ti-Al [40]. The composition of solids of these suspensions can only be formulated knowing the mass loss that both GO and prGO will undergo

during SPS. Consequently, pellets of GO and prGO were compacted individually, weighed, and heated with the SPS furnace up to 1900 °C in vacuum, and re-weighed, determining that their mass losses were ~54.4 and 42.5%, respectively. As expected, GO lost more weight (~12%) than prGO, attributable to its greater abundance of oxygen-containing functional groups. Consequently, to obtain the desired B_4C composites with 4.9 vol.% Ti-Al and 2 vol.% rGO one needs to prepare concentrated suspensions with compositions in wt.% of 89.07B_4C+7.02Ti-Al+3.91GO and of 89.82B_4C+7.08Ti-Al+3.10prGO.

Unfortunately, the attempts to prepare these suspensions to total solids loadings of 30 and 25 vol.% were unsuccessful because, as shown in Figs. 3A-B, during the gradual addition of GO/prGO the suspensions coagulated as grainy solids. In this scenario, aqueous colloidal processing is unfeasible. Fortunately, however, the situation changed when the total solids loading was reduced to 20 vol.%, in which case it was possible to prepare the desirable flowable suspensions, as shown in Fig. 3C.

The concentrated suspensions (20 vol.% of total solids) of 89.07B_4C+7.02Ti-Al+3.91GO and 89.82B_4C+7.08Ti-Al+3.10prGO were then characterized rheologically before and after sonication for various times. The objective was to identify the optimal co-dispersion conditions of B_4C and Ti-Al with GO/prGO platelets as coarse/fine as possible (for fabricating the orthotropic/isotropic composites). Fig. 4 shows the flow curve of the concentrated suspension of B_4C+Ti-Al+GO prepared only by mechanical agitation. This suspension exhibits a shear-thinning rheological behaviour (i.e., pseudo-plastic behaviour without yield point) with some thixotropy, indicative of good dispersion. The visual observations shown in Fig. 4 confirmed that it is indeed very flowable. This suspension has then the sought-for good dispersion of the B_4C, Ti-Al, and GO, while preserving the coarse nature of the starting flaky GO platelets.

Consequently, this suspension was freeze-dried, thus obtaining the starting powder mixture from which orthotropic B_4C/rGO composites would be fabricated. Note that in this case sonication is detrimental because it will re-exfoliate and re-fragment the desired flaky coarse GO platelets. Certainly, the flow curves shown in Fig. 4 for the concentrated suspensions of B_4C+Ti-Al+GO sonicated for 1 and 2 min confirm that this is what occurs. It is seen that the sonicated suspensions exhibit a very shear-thinning rheological behaviour (i.e., plastic behaviour with yield point), with an increasing yield stress. The direct visual observations shown in Fig. 4 confirmed that they are thicker and indeed resemble pastes. What happens is that sonication results in a greater number of thinner and smaller, but still relatively coarse, GO platelets, which, at rest conditions, are randomly oriented within the suspension between the B_4C and Ti-Al particles. Owing to their high aspect ratio, larger number, and random orientation, these newly-formed GO platelets offer a great overall resistance to the flow for low shear rates to such an extent that the suspension has a yield stress. However, shearing above the yield stress orients the GO platelets in parallel to the flow direction, thus reducing the suspension's viscosity.

Fig. 5 shows the flow curves of the concentrated suspension of B_4C+Ti-Al+prGO as a function of the sonication time. Unlike before, sonicating is now key to obtaining prGO platelets as fine as possible for fabricating the isotropic B_4C/rGO composites. It is seen that the sonicated suspensions exhibit the desired shear-thinning rheological behaviour with little thixotropy, whereas the non-sonicated suspension is more viscous and thixotropic. The direct visual observations shown in Fig. 5 confirmed that they are all fluid, although in this case sonication is indeed beneficial for the dispersion because the flow response got better. Most likely, this is because (*i*) the starting prGO platelets are much finer and smaller than the GO platelets, and become even much finer and smaller after sonication, and (*ii*) the concentrated suspensions

contain less prGO than GO because prGO loses less mass than GO during SPS. The optimal sonication time is 2 min, above which dispersion got worse (because the viscosity increases). This last is because the excess of sonication causes some re-agglomeration once the heat-induced surface activation starts to predominate over dispersion [41]. Consequently, the suspension sonicated for 2 min was freeze-dried thus obtaining the starting powder mixture from which isotropic B_4C/rGO composites would be fabricated.

3.2. Spark plasma sintering of orthotropic and isotropic B_4C/rGO composites

Figs. 6 and 7 present SEM images at different magnifications of the fracture surface of the B_4C composites fabricated by SPS from the optimized powder mixtures of B_4C+Ti-Al+GO and B_4C+Ti-Al+prGO, respectively. It is seen that the two composites are, thanks to the Ti-Al additives, well densified. Fig. 8 compares the Raman spectra of the composites and their powder mixtures, indicating that the former contains rGO nanoplatelets, not the parent GO/prGO nanoplatelets. This is because the intensity ratio of the D to G bands is lower in the composites, which is indicative of thermal reduction of GO/prGO to rGO *in situ* during SPS. The B_4C/rGO composites, however, exhibit notable microstructural differences regarding their distribution of nanoplatelets. Thus, the B_4C/rGO composite fabricated from B_4C+Ti-Al+GO is orthotropic because its rGO platelets are preferentially aligned in planes perpendicular to the pressing direction during SPS (Figs. 6A-B). Also, these rGO platelets are coarse and span longitudinally tens of microns because they are actually flaky aggregates of thick, large rGO nanoplatelets (Fig. 6C). On the contrary, it is hard to distinguish rGO platelets in the B_4C/rGO composite fabricated from B_4C+Ti-Al+prGO (Figs. 7A-B). Its microstructure is fairly isotropic because most of its

rGO platelets are fine and are randomly oriented (Figs. 7A-B) and wrapped at grain boundaries (Fig. 7C).

Interestingly, the two B_4C/rGO composites are equally superhard, with a Vickers hardness of ~31-32 GPa. They are therefore only slightly softer than the reference material without rGO, whose Vickers hardness is 34±1 GPa [40]. This is simply because rGO is relatively soft. However, as seen in the OM and SEM observations of Figs. 9 and 10, they exhibit marked differences in how the Vickers cracks propagated through their microstructures. Thus, in the orthotropic B_4C/rGO composite, the cracks run very little in parallel to the pressing direction during SPS because the flaky rGO platelets arrest their propagation (marked toughening), and much more in the perpendicular direction (virtually no toughening) (Figs. 9A and B). The anisotropic toughening power of the coarse rGO platelets is more evident in Figs. 9C and D, which show that no cracks are able to emanate from the corner of the plastic impression when this falls where there are coarse rGO platelets. In the isotropic B_4C/rGO composite, however, the Vickers cracks run equally in both directions (Fig. 10A), but they propagated tortuously (Fig. 10B), indicating active interaction with the thin rGO platelets and therefore moderate toughening. Indeed, recent detailed toughness measurements on Al_2O_3/rGO composites demonstrate that (*i*) those with orthotropic microstructure are markedly tough with a rising *R*-curve in the direction perpendicular to the rGO platelets, but are practically untoughened in the direction parallel to the rGO platelets [28], and that (*ii*) those with isotropic microstructure are moderately toughened in any direction with a shallower *R*-curve [28]. According to the Vickers indentation tests, this is the present case, and therefore future work (beyond the scope of this processing study) is needed to measure these *R*-curves.

Anisotropy in functional properties is also expected for the present orthotropic B_4C/rGO composites. Certainly, earlier study on orthotropic composites of B_4C reinforced with graphene platelets (GPLs) has demonstrated greater electrical conductivity in the direction parallel to the GPLs [33]. This is also true for orthotropic SiC/GPL composites [42], for which the thermal diffusivity has also been found to be greater in the direction parallel to the GPLs [43,44]. Higher electrical and/or thermal conductivities in parallel to the reinforcements have also been reported for Al_2O_3/GPL nanocomposites [45], and for AlN/GPL [46], 8YSZ/GPL [47], and 3YTZP/GPL composites [48], to name but a few examples.

What is remarkable is that the feasibility has been demonstrated of fabricating controllably by the same processing route B_4C/rGO composites with different microstructural designs, for their use on demand depending on the complexity of the mechanical loads and particular needs in each given engineering application. Also, this processing route is simple, and easily adaptable/extensible to make other orthotropic and isotropic ceramic/rGO composites (with the desired ceramic matrix, tailored content of sintering additives (if any), and required percentage of GO nanoplatelets), provided that all starting powders can be co-dispersible as concentrated suspensions (with shear-thinning rheological behaviour) conveniently deflocculated (using ideally a common deflocculant, or else a combination of various deflocculants of the same charge), in aqueous or non-aqueous media.

4. Conclusions

The processability of fully-dense B_4C/rGO composites with orthotropic and isotropic microstructural designs on demand has been studied. Based on the results and analyses, the following conclusions can be drawn:

1. A simple processing route combining aqueous colloidal processing with transient liquid-phase assisted SPS has been developed that is customizable to obtain both orthotropic and isotropic B_4C/rGO composites, controllably.
2. In this route, the orthotropic B_4C/rGO composites are obtained by using a source of coarse rGO platelets and imposing smooth co-dispersion conditions during aqueous colloidal processing to avoid their re-exfoliation/re-fragmentation.
3. Contrarily, the isotropic B_4C/rGO composites are obtained by using a source of fine rGO platelets and imposing intensive co-dispersion conditions to ensure their re-exfoliation/re-fragmentation.
4. Both types of B_4C/rGO composites are equally superhard (~31-32 GPa). Nonetheless, the orthotropic composites exhibit marked toughening and virtually no toughening for cracks propagating perpendicularly and in parallel to the rGO reinforcements, respectively. The isotropic composites exhibit however moderate toughening for any crack.

Acknowledgements. This work was supported by the Ministerio de Economía y Competitividad (Government of Spain) and FEDER Funds under the Grants nº MAT2016-76638-R and RTI2018-099033-B-C33. Financial support from the Junta de Extremadura under the Grant nº GR18149, also co-financed with FEDER Funds, is gratefully acknowledged as well. The authors thank Abalonyx AS for kindly providing the GO and prGO starting powders. Cristina Ojalvo thanks the Junta the Extremadura for funding her PhD Grant nº PD16027. Thanks are also due to Carmen Alcázar and María Díaz, at the Instituto de Cerámica y Vidrio, for their technical assistance.

References

1. F. Thevenot, Boron carbide – a comprehensive review, J. Eur. Ceram. Soc. 6 [4] (1990) 205–225.
2. M. Chen, J.W. McCauley, K.J. Hemker, Shock-induced localized amorphization in boron carbide, Science 299 (2003) 1563–1566.
3. H. Way, Media-milled nanoparticles boosts ceramic armor, Am. Ceram. Soc. Bull. 87 [5] (2008) 20–24.
4. A.K. Suri, C. Subramanian, J.K. Sonber, T.S.R.-Ch. Murthy, Synthesis and consolidation of boron carbide: a review, Int. Mater. Rev. 55 [1] (2010) 4–40.
5. V. Domnich, S. Reynaud, R.A. Haber, M. Chhowall, Boron carbide: structure, properties, and stability under stress, J. Am. Ceram. Soc. 94 [11] (2011) 3605–3628.
6. S. Leo, C. Tallon, G.V. Franks, Near-net-shaping methods for ceramic elements of (body) armor systems, J. Am. Ceram. Soc. 97 [10] (2014) 3013–3033.
7. D. Hallam, A. Heaton, B. James, P. Smith, J. Yeomans, The correlation of indentation behaviour with ballistic performance for spark plasma sintered armour ceramics, J. Eur. Ceram. Soc. 35 [8] (2015) 2243–2252.
8. B.M. Moshtaghioun, D. Gómez-García, A. Domínguez-Rodríguez, R.I. Todd, Abrasive wear rate of boron carbide ceramics: influence of microstructural and mechanical aspects on their tribological response, J. Eur. Ceram. Soc. 36 [16] (2016) 3925–3928.
9. S. Hayun, Reaction-bonded boron carbide for lightweight armor: the interrelationship between processing, microstructure, and mechanical properties, Am. Ceram. Soc. Bull. 96 [6] (2017) 22–29.
10. A.L. Ortiz, V.M. Candelario, O. Borrero-López, F. Guiberteau, Sliding-wear resistance of

pure near fully-dense B_4C under lubrication with water, diesel fuel, and paraffin oil, J. Eur. Ceram. Soc. 38 [4] (12018) 1158–1163.

11. S.L. Dole, S. Prochazka, R.H. Doremus, Microstructural coarsening during sintering of boron carbide, J. Am. Ceram. Soc. 72 [6] (1989) 958–966.
12. B.M. Moshtaghioun, D. Gómez-García, A. Domínguez-Rodríguez, R.I. Todd, Grain size dependence of hardness and fracture toughness in pure near fully-dense boron carbide ceramics, J. Eur. Ceram. Soc. 36 [7] (2016) 1829–1834.
13. F. Rodríguez-Rojas, R. Moreno, F. Guiberteau, AL. Ortiz, Aqueous colloidal processing of near-net shape B_4C–Ni cermet compacts, J. Eur. Ceram. Soc. 36 [8] (2016) 1915–1921.
14. A.L. Ortiz, V.M. Candelario, R. Moreno, F. Guiberteau, Near-net shape manufacture of B_4C–Co and ZrC–Co composites by slip casting and pressureless sintering, J Eur. Ceram. Soc. 37 [15] (2017) 4577–4584.
15. B.M Moshtaghioun, A.L. Ortiz, D. Gómez-García, A. Domínguez-Rodríguez, Toughening of super-hard ultra-fine grained B_4C densified by spark-plasma sintering via SiC addition, J Eur. Ceram. Soc. 33 [8] (2013) 1395–1401.
16. B.M. Moshtaghioun, F.L. Cumbrera, A.L. Ortiz, M. Castillo-Rodríguez, D. Gómez-García, Additive-free superhard B_4C with ultrafine-grained dense microstructures, J. Eur. Ceram. Soc. 34 [3] (2014) 841–848.
17. B.M. Moshtaghioun, A.L. Ortiz, D. Gómez-García, A. Domínguez-Rodríguez, Densification of B_4C nanopowder with nanograin retention by spark-plasma sintering, J. Eur. Ceram. Soc. 35 [6] (2015) 1991–1998.
18. B.M. Moshtaghioun, D. Gómez-García, A. Domínguez-Rodríguez, A.L. Ortiz, Enhancing the spark-plasma sinterability of B_4C nanopowders via room-temperature methylation

induced purification, J. Eur. Ceram. Soc. 36 [11] (2016) 2843–2848.

19. A.L. Ortiz, F. Sánchez-Bajo, V.M. Candelario, F. Guiberteau, Comminution of B_4C powders with a high-energy mill operated in air in dry or wet conditions and its effect on their spark-plasma sinterability, J. Eur. Ceram. Soc. 37 [13] (2017) 3873–3884.
20. C. Ojalvo, F. Guiberteau, A.L. Ortiz, Fabricating toughened super-hard B_4C composites at lower temperature by transient liquid-phase assisted spark plasma sintering with $MoSi_2$ additives, J. Eur. Ceram. Soc. 39 [9] (2019) 2862–2873.
21. B.R. Lawn. Fracture of brittle solids - second edition. Cambridge University Press, UK, 1993.
22. J.B. Wachtman. Mechanical properties of ceramics. John Wiley and Sons, US, (1996).
23. V.M. Candelario, O. Borrero-López, F. Guiberteau, R. Moreno, A.L. Ortiz, Sliding-wear resistance of liquid-phase-sintered SiC containing graphite nanodispersoids, J. Eur. Ceram. Soc. 34 [10] (2014) 2597–2602.
24. E. Zapata-Solvas, D. Gómez-García, A. Domínguez-Rodríguez, Towards physical properties tailoring of carbon nanotubes-reinforced ceramic matrix composites, J. Eur. Ceram. Soc. 332 [12] (2012) 3001–3020.
25. N.P. Padture, Multifunctional composites of ceramics and single-wall carbon nanotubes, Adv. Mater. 21 [17] (2009) 1767–1770.
26. Y. Liu, C. Ramirez, L. Zhang, W. Wu, N.P. Padture, *In situ* direct observation of toughening in isotropic nanocomposites of alumina ceramic and multiwall carbon nanotubes, Acta Mater. 127 (2017) 203–210.
27. C. Ramirez, Q. Wang, M. Belmonte, P. Miranzo, M.I. Osendi, B.W. Sheldon, N.P. Padture, Direct in situ observation of toughening mechanisms in nanocomposites of silicon nitride

and reduced graphene-oxide, Scripta Mater. 149 (2018) 40–43.

28. Q. Wang, C. Ramirez, C.S. Watts, O. Borrero-Lopez, A.L. Ortiz, B.W. Sheldon, N.P. Padture, Fracture, fatigue, and sliding-wear behavior of nanocomposites of alumina and reduced graphene-oxide, Acta Mater. 186 (2020) 29–39.
29. M. Li, W. Wang, Q. He, A. Wang, L. Hu, Z. Fu, Reduced-graphene-oxide-reinforced boron carbide ceramics fabricated by spark plasma sintering from powder mixtures obtained by heterogeneous co-precipitation, Ceram. Int. 45 [13] (2019) 16496–16503.
30. L. Hu, W. Wang, Q. He, A. Wang, C.Liu, T. Tian, H. Wang, Z. Fu, Preparation and characterization of reduced graphene oxide-reinforced boron carbide ceramics by self-assembly polymerization and spark plasma sintering, J. Eur. Ceram. Soc. (2019) in press.
31. A. Kovalčíková, R. Sedlák, P. Rutkowski, J. Dusza, Mechanical properties of boron carbide+graphene platelet composites, Ceram. Int. 42 [1 Part B] (2016) 2094–2098.
32. R. Sedlák, A. Kovalčíková, J. Balko, P. Rutkowski, A. Dubiel, D. Zientara, V. Girman, E. Múdra, J. Dusza, Effect of graphene platelets on tribological properties of boron carbide ceramic composites, Int. J. Refract. Met. Hard Mater. 65 (2017) 57–63.
33. R. Sedlák, A. Kovalčíková, E. Múdra, P. Rutkowski, A. Dubiel, V. Girman, R. Bystrický, J. Dusza, Boron carbide/graphene platelet ceramics with improved fracture toughness and electrical conductivity, J. Eur. Ceram. Soc. 37 [12] (2017) 3773–3780.
34. P. Rutkowski, A. Dubiel, W. Piekarczyk, M. Ziabka, J. Dusza, Anisotropy in thermal properties of boron carbide-graphene platelet composites, J. Eur. Ceram. Soc. 36 [12] (2015) 3051–3057.
35. R. Alexander, T.S.R.Ch. Murthy, K.V. Ravikanth, J. Prakash, T. Mahata, S.R. Bakshi, M. Krishnan, K. Dasgupta, Effect of graphene nano-platelet reinforcement on the mechanical

properties of hot pressed boron carbide based composite, Ceram. Int. 44 [8] (2018) 9830–9838.

36. Y. Tan, H. Luo, H. Zhang, S. Peng, Graphene nanoplatelets reinforced boron carbide composites with high electrical and thermal conductivity, J. Eur. Ceram. Soc. 36 [11] (2016) 2679–2687.
37. Y. Tan, H. Zhang, S. Peng, Electrically conductive graphene nanoplatelet/boron carbide composites with high hardness and toughness, Scripta Mater. 114 (2016) 98–102.
38. W. Ji, R.I. Todd, W. Wang, H. Wang, J. Zhang, Z. Fu, Transient liquid phase spark plasma sintering of B_4C-based ceramics using Ti-Al intermetallics as sintering aid, J. Eur. Ceram. Soc. 36 [10] (2016) 2419–2426.
39. A.L. Ortiz, C.A. Galán, O. Borrero-López, F. Guiberteau, Highly sliding-wear resistant B_4C composites fabricated by spark-plasma sintering with Ti-Al additives, Scripta Mater 177 (2020) 91–95.
40. C. Ojalvo, R. Moreno, F. Guiberteau, A.L. Ortiz, Manufacturing B_4C parts with Ti-Al intermetallics by aqueous colloidal processing, J. Eur. Ceram. Soc. 40 [2] (2020) 226–233.
41. R. Moreno, Reología de suspensiones cerámicas, Consejo Superior de Investigaciones Científicas, Madrid, Spain, 2005.
42. B. Román-Manso, E. Domingues, F.M. Figueiredo, M. Belmonte, P. Miranzo, Enhanced electrical conductivity of silicon carbide ceramics by addition of graphene nanoplatelets, J. Eur. Ceram. Soc. 35 [10] (2015) 2723–2731.
43. O. Hanzel, R. Sedlák, J. Sedláček, V. Bizovská, R. Bystrický, V. Girman, A. Kovalčíková, J. Dusza, P. Šajgalík, Anisotropy of functional properties of SiC composites with GNPs, GO and in-situ formed graphene, J. Eur. Ceram. Soc. 37 [12] (2017) 3731–3739.

44. B. Román-Manso, Y. Chevillotte, M.I. Osendi, M. Belmonte, P. Miranzo, Thermal conductivity of silicon carbide composites with highly oriented graphene nanoplatelets, J. Eur. Ceram. Soc. 36 [16] (2016) 3987–3993.

45. Y. Çelik, A. Çelik, E. Flahaut, E. Suvaci, Anisotropic mechanical and functional properties of graphene-based alumina matrix nanocomposites, J. Eur. Ceram. Soc. 36 [8] (2016) 2075–2086.

46. S. Baskut, A. Cinar, S. Turan, Directional properties and microstructures of spark plasma sintered aluminum nitride containing graphene platelets, J. Eur. Ceram. Soc. 37 [12] (2017) 3759–3772.

47. A. Gómez-Gómez, C. Ramírez, J. Llorente, A. Garcia, P. Moreno, H. Reveron, J. Chevalier, M.I. Osendi, M. Belmonte, P. Miranzo, Improved crack resistance and thermal conductivity of cubic zirconia containing graphene nanoplatelets, J. Eur. Ceram. Soc. 40 [4] (2020) 1557–1565.

48. A. Gallardo-López, I. Márquez-Abril, A. Morales-Rodríguez, A. Muñoz, R. Poyato, Dense graphene nanoplatelet/yttria tetragonal zirconia composites: processing, hardness and electrical conductivity, Ceram. Int. 43 [15] (2017) 11743–111752.

Figure Captions

Figure 1. Dependence of the zeta potential on pH and PEI deflocculant content for the individual dilute suspensions of GO, as indicated. Dots are the experimental data, and the lines are guides for the eye. The grey stripe denotes the zone excluded for low colloidal stability. The blue stripe denotes the zones excluded for restrictions of charge sign or pH. The curves of zeta potential for B_4C and Ti-Al with 1 wt.% PEI are also included as references for the co-dispersion [40].

Figure 2. Dependence of the zeta potential on pH and PEI deflocculant content for the individual dilute suspensions of prGO, as indicated. Dots are the experimental data, and the lines are guides for the eye. The grey stripe denotes the zone excluded for low colloidal stability. The blue stripe denotes the zones excluded for restrictions of charge sign or pH. The curves of zeta potential for B_4C and Ti-Al with 1 wt.% PEI are also included as references for the co-dispersion [40].

Figure 3. Optical photographs showing the visual appearance directly observable just after dispersing the entire amount of prGO into the water for total solids loadings of (A) 30, (B) 25, and (C) 20 vol.%.

Figure 4. Flow curves as a function of sonication time for the $89.07B_4C+7.02$Ti-Al$+3.91$GO concentrated suspension prepared to 20 vol.% total solids, and optical photographs showing its visual appearance. Sonication was not prolonged further once the flow curve worsened. The number at the right of each curve denotes the sonication time. The arrows indicate the uploading and downloading stretches of the flow curves.

Figure 5. Flow curves as a function of sonication time for the 89.82B_4C+7.08Ti-Al+3.10prGO concentrated suspension prepared to 20 vol.% total solids, and optical photographs showing its visual appearance. Sonication was not prolonged further once the flow curve worsened. The number at the right of each curve denotes the sonication time. The arrows indicate the uploading and downloading stretches of the flow curves.

Figure 6. SEM micrographs of B_4C/rGO composite fabricated from the optimal B_4C+Ti-Al+GO concentrated suspension showing its orthotropic microstructure at magnifications of (A) 1000×, (B) 5000×, and (C) 5000× but with detail of the flaky rGO platelets at 11500×. The vertical arrows mark the pressing direction during SPS.

Figure 7. SEM micrographs of B_4C/rGO composite fabricated from the optimal B_4C+Ti-Al+prGO concentrated suspension showing its isotropic microstructure at magnifications of (A) 1000×, (B) 5000×, and (C) 65000×. The vertical arrows mark the pressing direction during SPS.

Figure 8. Raman spectra of the two B_4C/rGO composites fabricated by SPS, and of their starting B_4C+Ti-Al+GO and B_4C+Ti-Al+rpGO powder mixtures. The position of the bands D, G, and 2D are indicated.

Figure 9. Optical and SEM micrographs of the Vickers cracks in the orthotropic B_4C/rGO ceramic showing (A) a general view, (B) a vertical crack being arrested at coarse rGO platelets. and (C-D) residual impressions with their top corners located at coarse GO platelets. The plastic impression is coloured with light-violet background. The vertical arrows mark the pressing

direction during SPS. These Vickers indentation tests were performed on the polished cross-section surface.

Figure 10. Optical and SEM micrographs of the Vickers cracks in the isotropic B_4C/rGO ceramic showing (A) a general view and (B-C) details of the tortuous path of the horizontal and vertical cracks emanating from the corners of the residual impression. The plastic impression is coloured with light-violet background. The vertical and horizontal arrows mark the pressing direction during SPS. These Vickers indentation tests were performed on the polished cross-section surface.

Table and Table Caption

Table 1. Features of the starting powders. Purity, morphology, and size are as provided by the manufacturer's specifications. Densities were measured experimentally by He-pycnometry.

Powder	Purity (%)	Density (g/cm^3)	Morphology	Size (μm)
B_4C	>99	2.559	particulate	~0.7
Ti-Al	>99.8	3.841	particulate	~38
GO	>99	1.845	nanoplatelets	~10 diameter, 0.005 thickness
rGO	>99	2.372	nanoplatelets	~5 diameter, 0.002 thickness

Figure

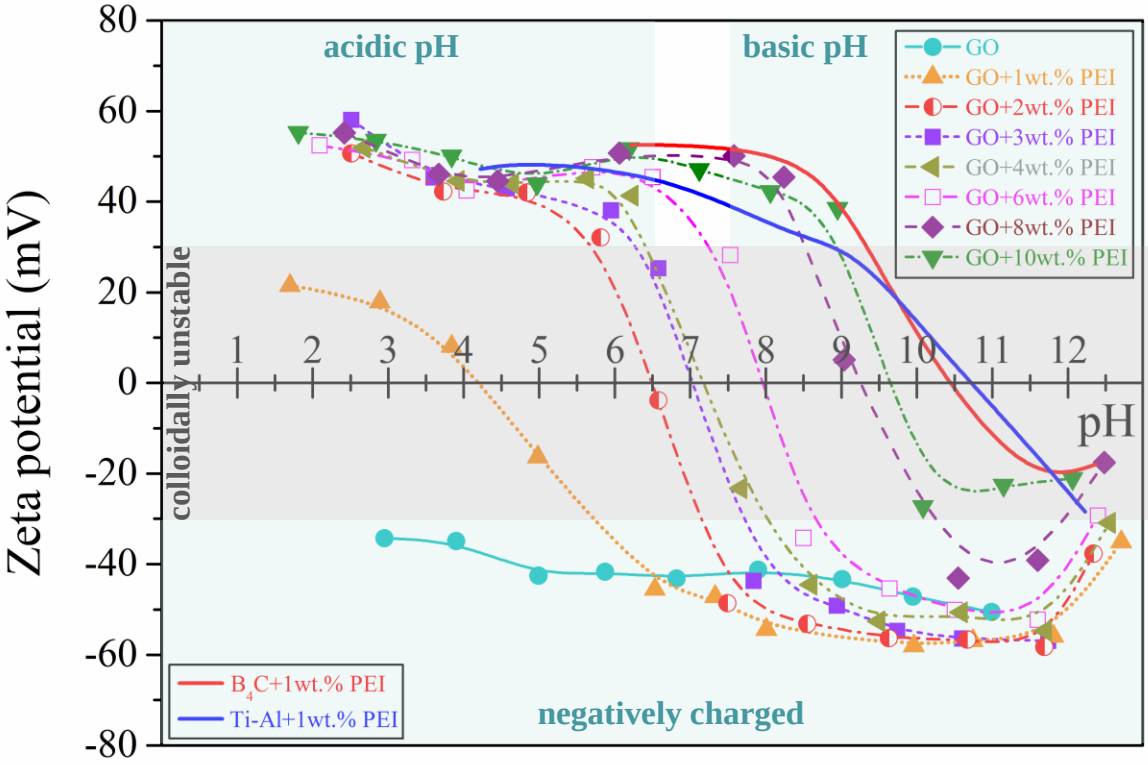

Ojalvo *et al.*
Figure 1

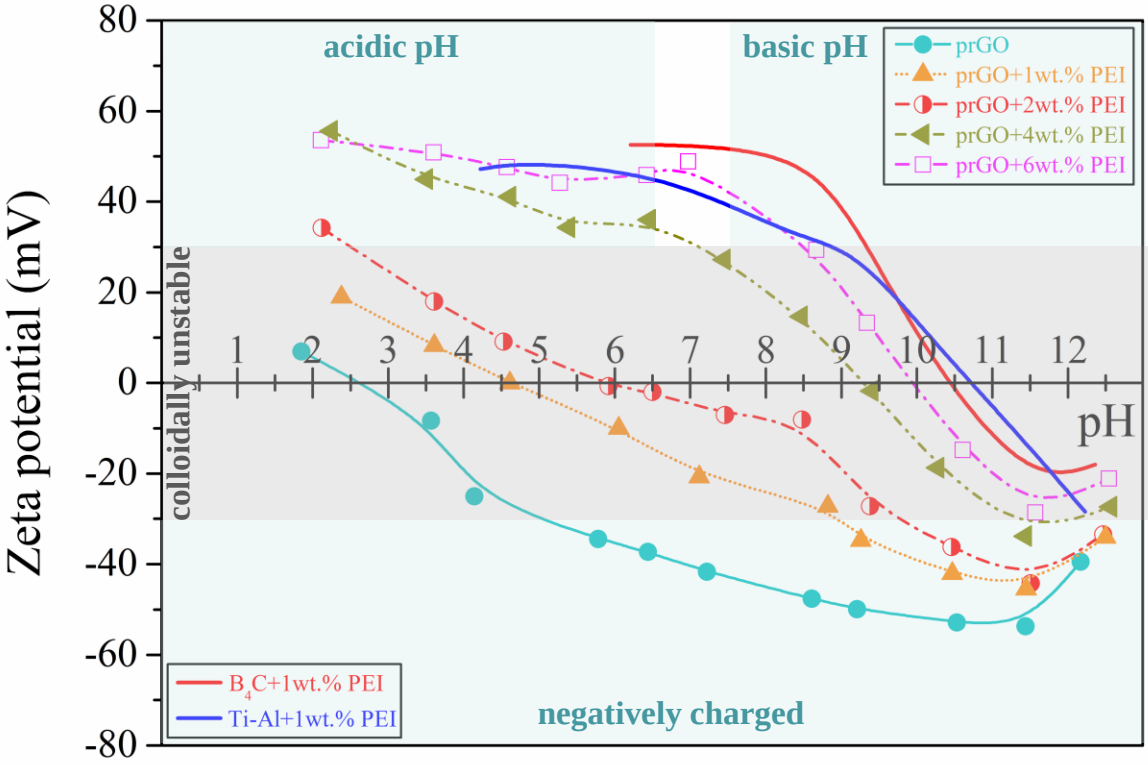

Ojalvo *et al.*
Figure 2

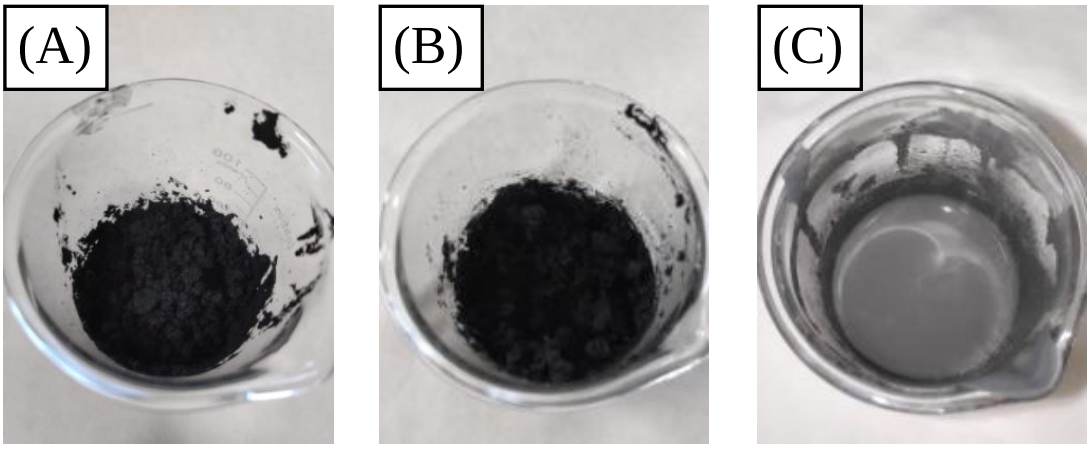

Ojalvo *et al.*
Figure 3

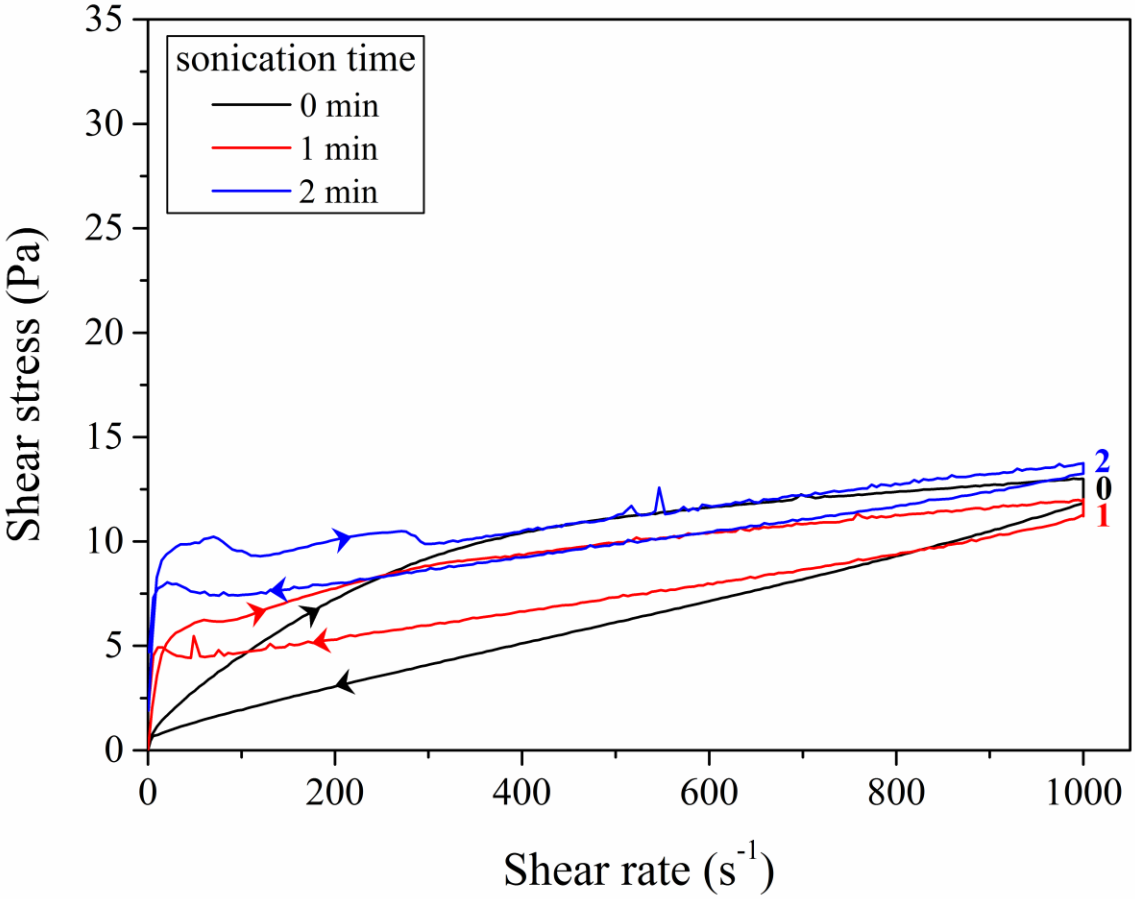

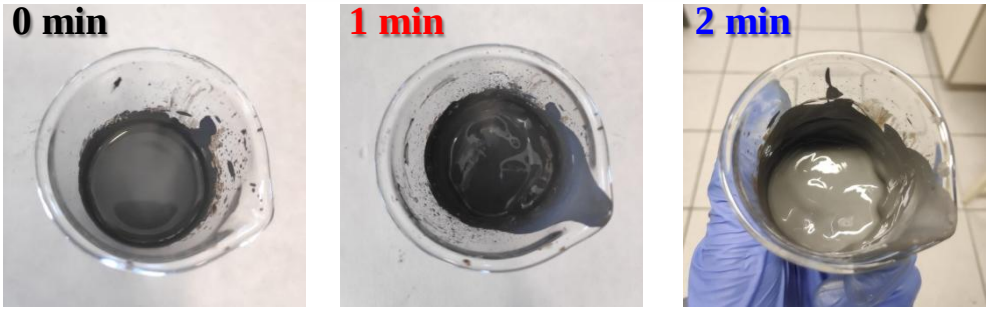

Ojalvo *et al.*
Figure 4

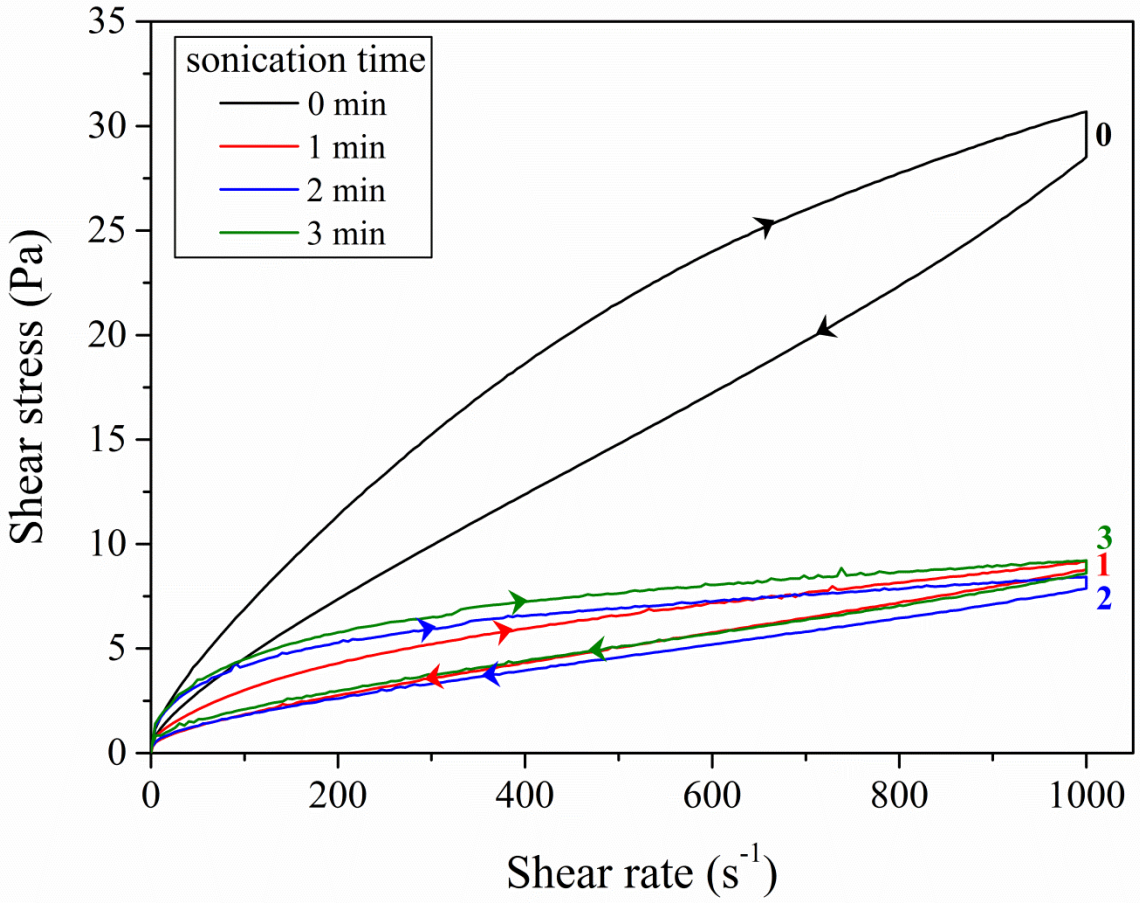

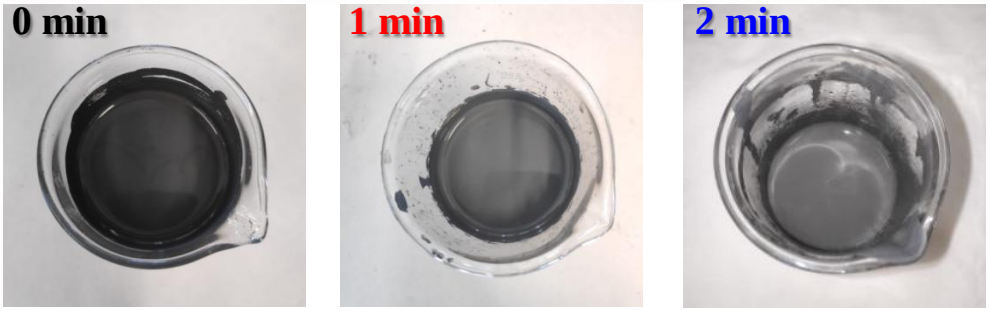

Ojalvo *et al.*
Figure 5

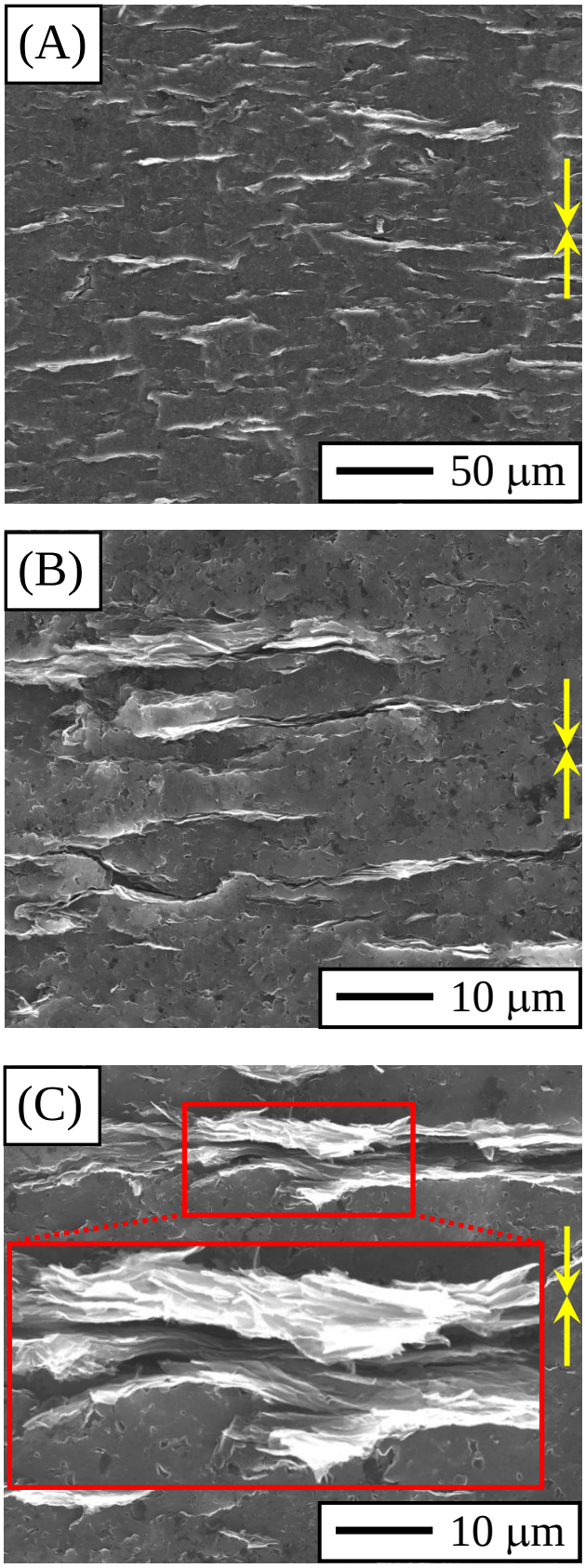

Ojalvo *et al.*
Figure 6

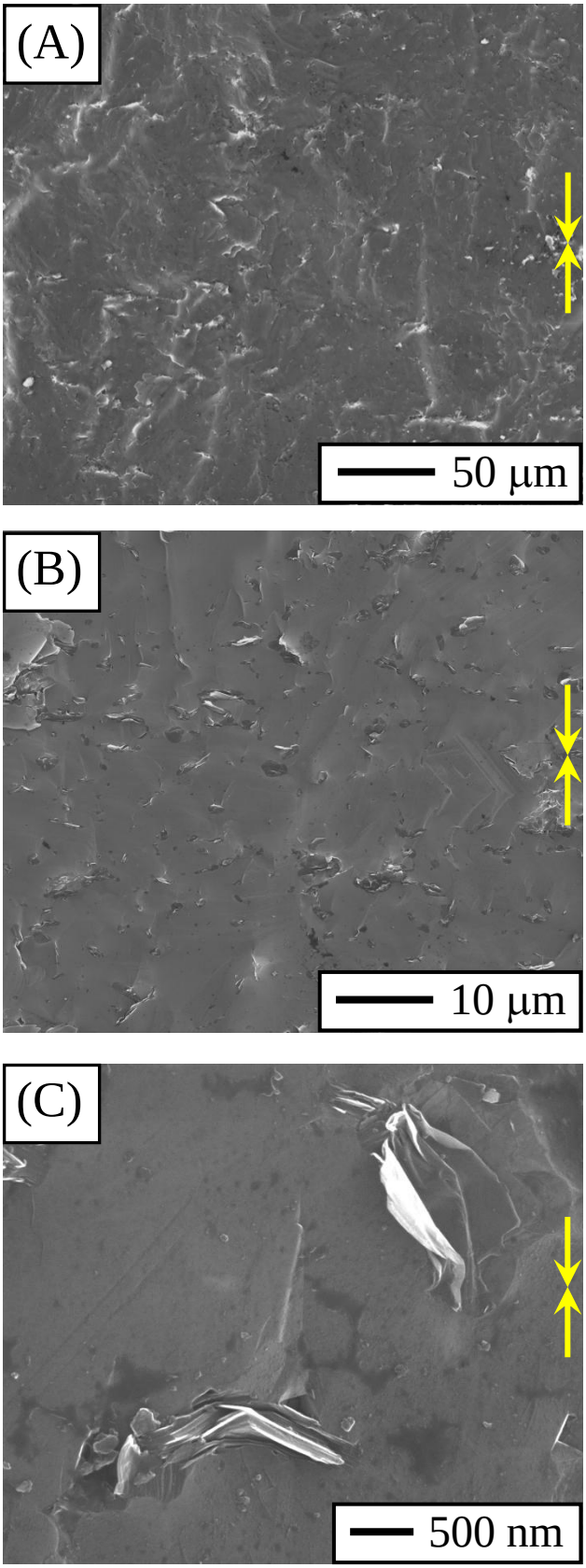

Ojalvo *et al.*
Figure 7

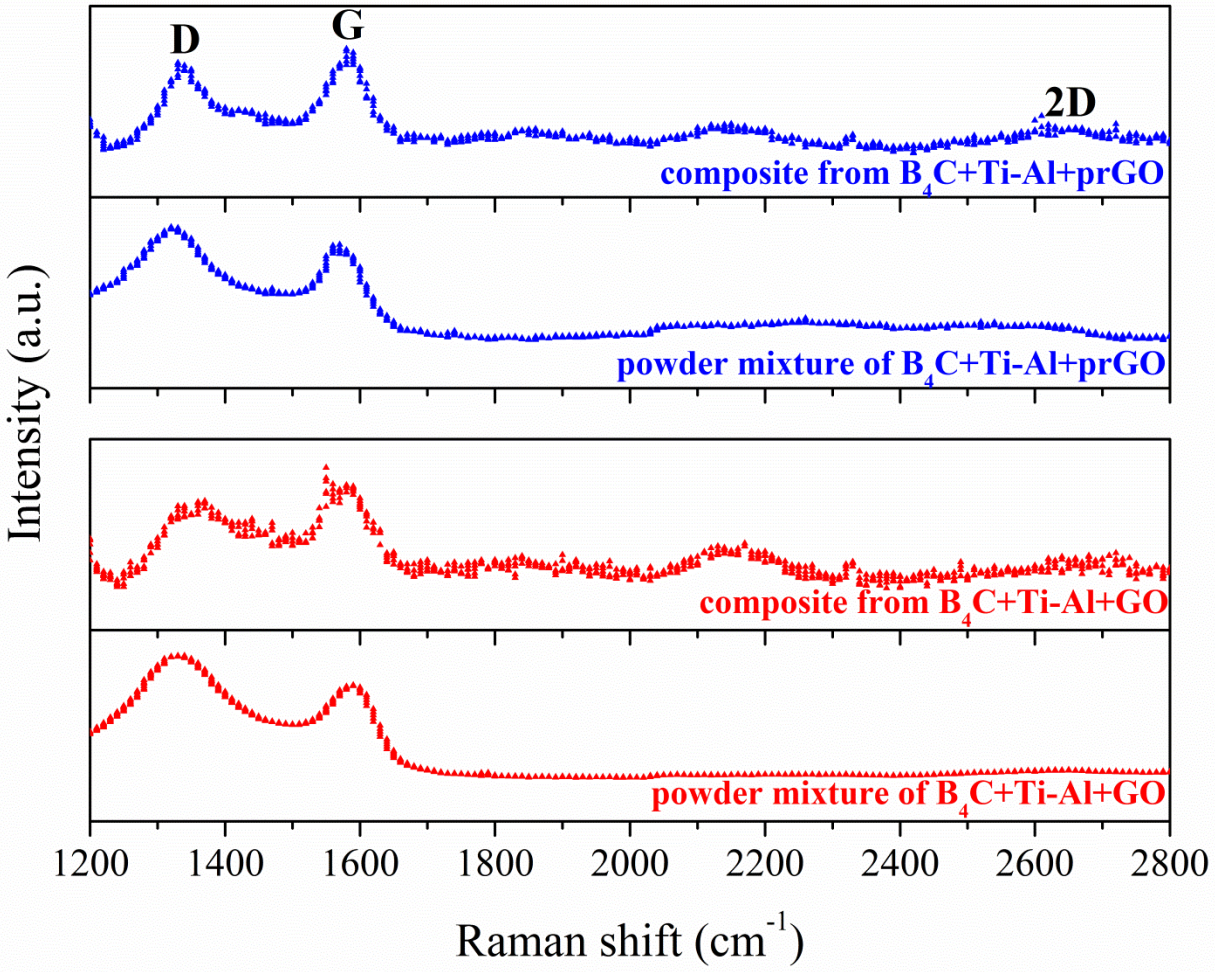

Ojalvo *et al.*
Figure 8

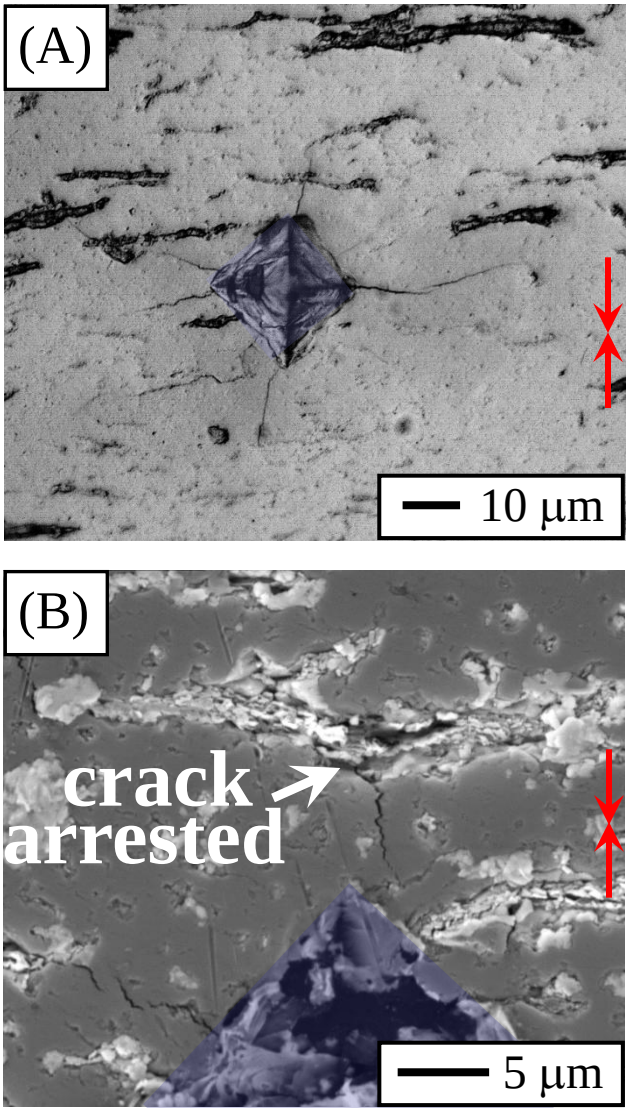

Ojalvo *et al.*
Figure 9

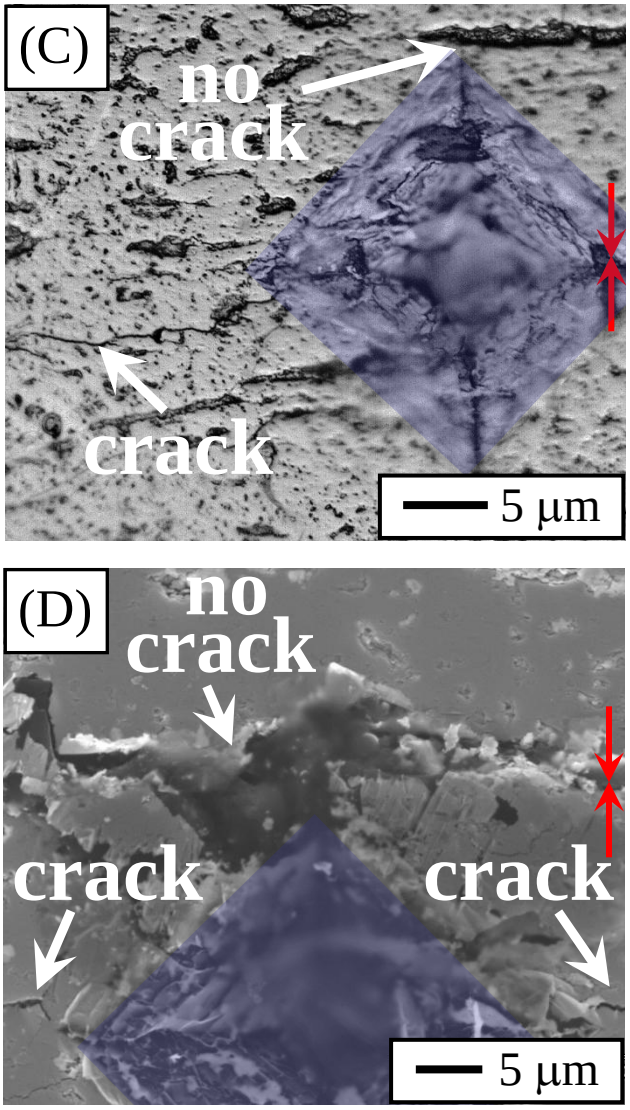

Ojalvo *et al.*
Figure 9

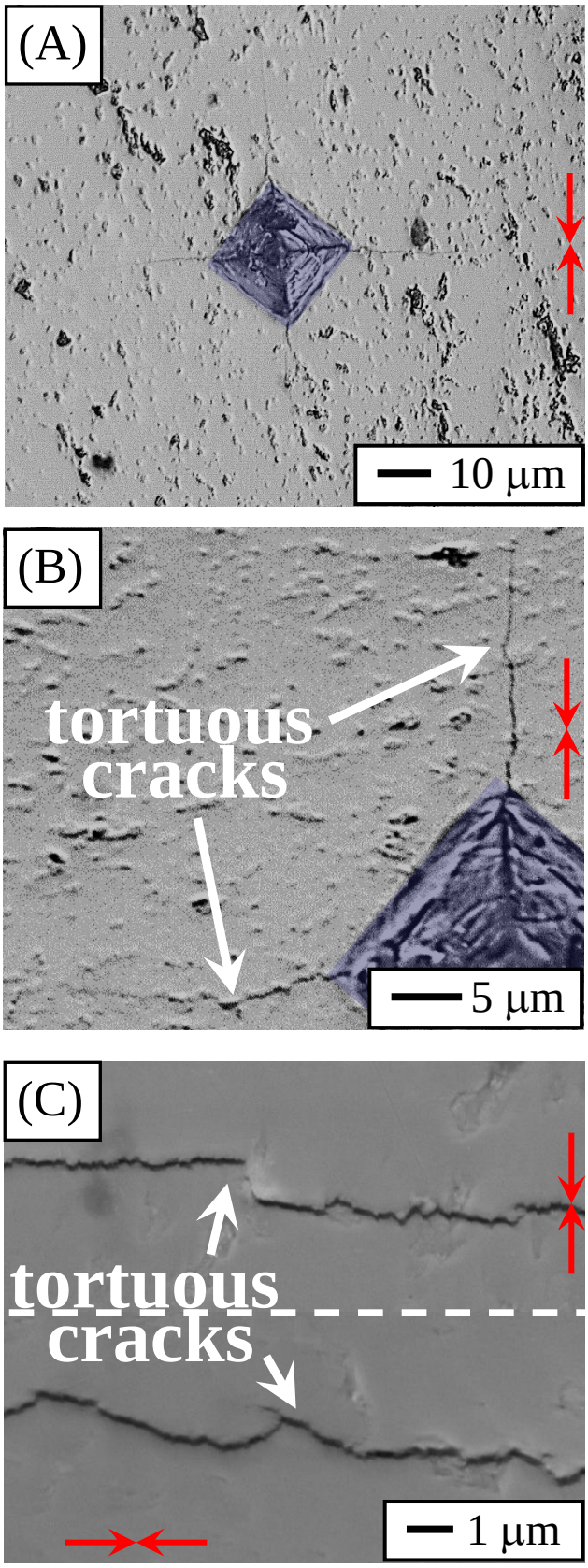

Ojalvo *et al.*
Figure 10

Figure Captions

Figure 1. Dependence of the zeta potential on pH and PEI deflocculant content for the individual dilute suspensions of GO, as indicated. Dots are the experimental data, and the lines are guides for the eye. The grey stripe denotes the zone excluded for low colloidal stability. The blue stripe denotes the zones excluded for restrictions of charge sign or pH. The curves of zeta potential for B_4C and Ti-Al with 1 wt.% PEI are also included as references for the co-dispersion [40].

Figure 2. Dependence of the zeta potential on pH and PEI deflocculant content for the individual dilute suspensions of prGO, as indicated. Dots are the experimental data, and the lines are guides for the eye. The grey stripe denotes the zone excluded for low colloidal stability. The blue stripe denotes the zones excluded for restrictions of charge sign or pH. The curves of zeta potential for B_4C and Ti-Al with 1 wt.% PEI are also included as references for the co-dispersion [40].

Figure 3. Optical photographs showing the visual appearance directly observable just after dispersing the entire amount of prGO into the water for total solids loadings of (A) 30, (B) 25, and (C) 20 vol.%.

Figure 4. Flow curves as a function of sonication time for the $89.07B_4C$+7.02Ti-Al+3.91GO concentrated suspension prepared to 20 vol.% total solids, and optical photographs showing its visual appearance. Sonication was not prolonged further once the flow curve worsened. The number at the right of each curve denotes the sonication time. The arrows indicate the uploading and downloading stretches of the flow curves.

Figure 5. Flow curves as a function of sonication time for the 89.82B_4C+7.08Ti-Al+3.10prGO concentrated suspension prepared to 20 vol.% total solids, and optical photographs showing its visual appearance. Sonication was not prolonged further once the flow curve worsened. The number at the right of each curve denotes the sonication time. The arrows indicate the uploading and downloading stretches of the flow curves.

Figure 6. SEM micrographs of B_4C/rGO composite fabricated from the optimal B_4C+Ti-Al+GO concentrated suspension showing its orthotropic microstructure at magnifications of (A) 1000×, (B) 5000×, and (C) 5000× but with detail of the flaky rGO platelets at 11500×. The vertical arrows mark the pressing direction during SPS.

Figure 7. SEM micrographs of B_4C/rGO composite fabricated from the optimal B_4C+Ti-Al+prGO concentrated suspension showing its isotropic microstructure at magnifications of (A) 1000×, (B) 5000×, and (C) 65000×. The vertical arrows mark the pressing direction during SPS.

Figure 8. Raman spectra of the two B_4C/rGO composites fabricated by SPS, and of their starting B_4C+Ti-Al+GO and B_4C+Ti-Al+rpGO powder mixtures. The position of the bands D, G, and 2D are indicated.

Figure 9. Optical and SEM micrographs of the Vickers cracks in the orthotropic B_4C/rGO ceramic showing (A) a general view, (B) a vertical crack being arrested at coarse rGO platelets. and (C-D) residual impressions with their top corners located at coarse GO platelets. The plastic impression is coloured with light-violet background. The vertical arrows mark the pressing

direction during SPS. These Vickers indentation tests were performed on the polished cross-section surface.

Figure 10. Optical and SEM micrographs of the Vickers cracks in the isotropic B_4C/rGO ceramic showing (A) a general view and (B-C) details of the tortuous path of the horizontal and vertical cracks emanating from the corners of the residual impression. The plastic impression is coloured with light-violet background. The vertical and horizontal arrows mark the pressing direction during SPS. These Vickers indentation tests were performed on the polished cross-section surface.

Table and Table Caption

Table 1. Features of the starting powders. Purity, morphology, and size are as provided by the manufacturer's specifications. Densities were measured experimentally by He-pycnometry.

***Summary of Novel Conclusions**

- A fabrication route based on aqueous colloidal processing plus transient liquid-phase assisted spark-plasma-sintering (SPS) with Ti-Al additives is described for the environmentally friendly obtention of superhard B_4C composites reinforced with reduced graphene oxide (rGO) having orthotropic and isotropic microstructures.
- Orthotropic B_4C/rGO composites, which have coarse rGO platelets preferentially aligned perpendicular to the SPS pressing direction, are prepared from mixtures of B_4C and Ti-Al particles with a source of thick, large rGO nanoplatelets by imposing smooth co-dispersion conditions to avoid platelet re-exfoliation and fragmentation.
- Isotropic B4C/rGO composites, which have fine rGO platelets randomly oriented, are fabricated from mixtures of B_4C and Ti-Al particles with a source of thin, small rGO nanoplatelets by applying intensive sonication to promote platelet re-exfoliation and fragmentation during co-dispersion.
- The orthotropic and isotropic B_4C/rGO composites are equally superhard, but their microstructures interact differently with the cracks.